



The anodic dissolution of pyrite (FeS_2) in hydrochloric acid solutions



L.J. Bryson^a, F.K. Crundwell^{b,*}

^a Anglo American Technical Solutions, South Africa

^b CM Solutions (Pty) Ltd., South Africa

ARTICLE INFO

Article history:

Received 16 July 2013

Received in revised form 11 January 2014

Accepted 14 January 2014

Available online 21 January 2014

Keywords:

Pyrite

Dissolution

Anodic dissolution

Leaching

Acid mine drainage

ABSTRACT

Pyrite is an abundant mineral, and its dissolution is important in the formation of acid mine drainage and the extraction of metals. It has also been considered as a candidate material for electrochemical solar cells. We studied the anodic processes on pyrite in hydrochloric acid. The current–voltage curve at steady state has three regions. At potentials below 0.6 V, the current is low, and the Tafel slope is high; between 0.6 and 0.9 V, the current is significant, and the Tafel slope is 0.082 V/decade; at potentials above 0.9 V, the current remains high, but the Tafel slope changes to 0.430 V/decade. From careful measurements of the dissolution of pyrite by chlorine, we show that this third region is due to charge transfer and not ohmic resistance. The shape of the current–voltage curve is unaffected by the type of acid used. The effect of temperature was measured, and the activation energies for the middle and upper region are 46 and 105 kJ/mol, respectively. The steady-state current–voltage curves are not affected by the concentration of HCl, but are affected by the concentration of chloride ions, with an order of reaction of -0.1 , indicating that the rate is only slightly dependent on chloride ions. Pretreatment tests and XPS analysis of the surface confirm that the change in Tafel slope is not due to the formation of a surface coating or oxidation product. A comprehensive model of the anodic dissolution of pyrite that describes the current–voltage behavior of pyrite over the entire anodic region is proposed. At low potentials, the behavior of pyrite is typical of an n-type semiconductor with some dissolution. However, as the potential is increased, the Fermi level overlaps with an intrinsic surface state. The rate of dissolution of the pyrite in this region is dependent on the occupancy of the surface state. This accounts for previous reports indicating that pyrite is quasi-metallic. The rate-determining step is the transfer of charge across the space-charge layer. As the potential is increased to about 0.9 V, the surface state is unoccupied, and the rate-determining step changes to the transfer of ions across the Helmholtz layer. An expression based on this model fits the experimental data. An important feature of this model is that it also explains two contradictory features of pyrite electrochemistry. On the one hand, n-type and p-type pyrite samples may have similar kinetic parameters, which suggests that the electronic structure of pyrite makes little difference. On the other hand, illuminating the sample with light increases the rate of dissolution, which suggests that the electronic structure is important. The proposed model based on surface states explains these seemingly contradictory observations.

© 2014 Elsevier B.V. All rights reserved.

1. Introduction

The oxidation of pyrite is important in a number of different fields. In the extraction of gold, the dissolution of pyrite exposes enclosed gold. Cobalt is incorporated into the pyrite structure in some ores (Dew et al., 1997). Extraction of cobalt from these ores requires dissolution of the pyrite structure (Fowler et al., 1999, 2001; Holmes and Crundwell, 2000; Holmes et al., 1999). The dissolution of pyrite is very important in the generation of acid mine and rock drainage. Exposure of pyrite exposed by industrial activity and its subsequent dissolution can lead to major environmental problems (Evangelou, 1995). Other environmental problems, such as the high levels of sulfur dioxide emission from coal-fired power stations may be prevented by the removal of

pyrite from coal by oxidative dissolution (Mishra and Osseo-Asare, 1987).

Two of the properties of pyrite, its ability to absorb light in the whole of the visible spectrum and its low rate of anodic photocorrosion, suggest that it may be a suitable material for the anode in a photoelectrochemical cell (Chen et al., 1991; Schubert and Tributsch, 1990; Wei and Osseo-Asare, 1996, 1997). Photoelectrochemical studies of the pyrite–aqueous solution interface have shown that pyrite is an efficient photoanode and that corrosion by photoinduced holes is suppressed by the non-bonding d-states (Chen et al., 1991; Crundwell, 1988; Ennaoui et al., 1985, 1986; Mishra and Osseo-Asare, 1992; Schubert and Tributsch, 1990).

Because of the importance of the oxidation of pyrite in these fields, the electrochemistry of pyrite has attracted the attention of many investigators.

Characterizing the pyrite–solution interface by the analysis of the capacitance using Mott–Schottky plots has not been successful with

* Corresponding author.

E-mail address: frank.crundwell@cm-solutions.co.za (F.K. Crundwell).

pyrite in aqueous solutions. This is due to interference from the adsorption of solution species or intrinsic states on the surface (Mishra and Osseo-Asare, 1988a, 1988b, 1992). The characterization of the interface may be performed in non-aqueous solutions to limit the effect of adsorption surface states (Frank and Bard, 1975; Kohl and Bard, 1977). However, Mott–Schottky plots of pyrite are non-linear even in acetonitrile solutions (Mishra and Osseo-Asare, 1988a, 1988b). Therefore, it appears that the surface properties of pyrite are far more complex than those of ideal and more conventional semiconductors (Salvador et al., 1991).

The ideal semiconductor-solution interface and the Schottky-barrier diode are analogous (Koval and Howard, 1992; Morrison, 1980; Reichman, 1980; Vanmaekelbergh, 1997). Thus, large anodic currents due to dissolution are not expected for a wide bandgap, n-type semiconductor in an indifferent electrolyte in the dark (Vanden Berghe et al., 1974). The expected current–voltage curve for an ideal n-type semiconductor is shown in Fig. 1.

If pyrite behaved in this ideal manner, the current due to the anodic dissolution of n-type pyrite expected to be low. In acetonitrile solutions, pyrite behaves as an ideal semiconductor: only very small anodic currents are found in this blocked region (Mishra and Osseo-Asare, 1992). However, significant anodic currents are measured at potentials above 0.6 V (vs Ag/AgCl)¹ for pyrite in aqueous solutions, suggesting that the non-ideal behavior of pyrite is associated with the adsorption of water-related species. In other words, the dissolution of pyrite is associated with adsorbed hydroxyl or hydronium species.

A number of studies have examined the characteristics of the current–voltage curve, and the chemistry of the corrosion products (Ahlberg and Broo, 1997; Biegler and Swift, 1979; Meyer, 1979; Peters and Majima, 1967; Springer, 1970). Two potential regions have been identified in the anodic current–voltage curve. These two regions correspond with the two regions shaded in gray in Fig. 1.

In the first region, between the rest potential and about 0.6 V, the current is very low. The formation of a protective coating of either sulfur or polysulfide material has been advanced as an explanation for these low currents in this region (Biegler and Swift, 1979). However, Crundwell (1988) argued that the electronic structure of pyrite was responsible for the current behavior in this region.

In the second region, between 0.6 and 0.9 V, significant currents are measured with a Tafel slope of between 0.09 and 0.11 V/decade (Ahlberg and Broo, 1997; Biegler and Swift, 1979; Meyer, 1979; Peters and Majima, 1967; Springer, 1970). The value of the Tafel slope falls between that of an ideal semiconductor (0.06 V) and a metal (0.12 V). However, Springer (1970) and Biegler and Swift (1979) found that type of conductivity (n or p-type) had no effect on the Tafel slope. Furthermore, Doyle and Mirza (1996) could find no correlation between the kinetics of anodic dissolution and the bulk electronic properties of pyrite. Thus, these researchers found that the electronic properties have little effect on the breakdown, or dissolution, of the semiconductor.

Two explanations for the value of the Tafel slope in the second region have been advanced. Meyer (1979) found that pH affected the rate of reaction and proposed a two-layer mechanism to account for both the Tafel slope and the effect of pH. The transfer of charge across the first layer is of the same form as the Butler–Volmer equation, while the transfer of charge across the second layer is an equilibrium process dependent on both the pH and the potential difference across this second layer. Biegler and Swift (1979) proposed that an electroadsorption step could account for the effect of pH. They proposed the coverage of the surface by the adsorbed species was described by the Temkin isotherm, and this accounted for the value of the Tafel slope. Both these studies treated the pyrite electrode as a metal.

Deviations from the ideal semiconductor model have been often attributed to the presence of surface states within the band gap of the

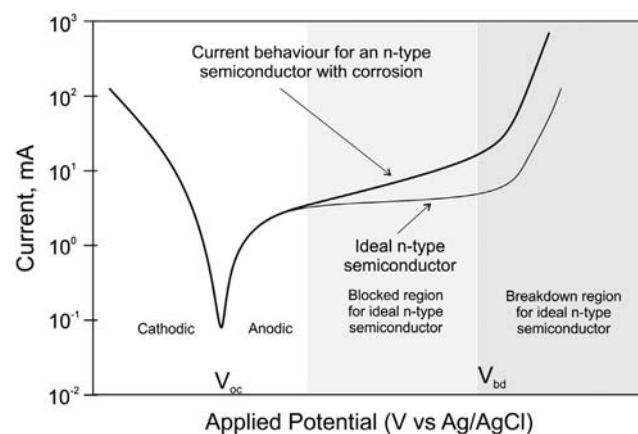


Fig. 1. The anodic behavior for an n-type semiconductor. With increasing potentials from the open-circuit potential, V_{oc} , the anodic behavior of an ideal n-type semiconductor becomes saturated, which means that the current is limited by the transport of electrons across the space charge layer. For a non-ideal semiconductor, the current isn't completely limited due to either dissolution (corrosion) of the semiconductor, or another conduction band process. As the anodic potential is increased, a point is reached when the semiconductor begins to breakdown. This breakdown is due to dissolution (corrosion) of the semiconductor.

semiconductor (Allongue and Cachet, 1985; Bard et al., 1980; Chazalviel, 1982; Disilverstro et al., 1986; Frese and Morrison, 1979; Li and Peter, 1985; Morrison, 1980; Noufi et al., 1978; Vandermolen et al., 1980). Such surface states may arise from unfilled valencies on surface atoms, or from adsorbed chemical species (Morrison, 1980). In order to avoid the formation of adsorbed surface states, the semiconductor surface may be characterized in non-aqueous solutions (Frank and Bard, 1975; Kohl and Bard, 1977). However, the Mott–Schottky plots of pyrite are non-linear even in non-aqueous solutions, suggesting that surface states are intrinsic states rather than adsorbed states. The photovoltaic behavior of pyrite in the presence of various redox couples suggested that the Fermi level is pinned by surface states since the potential at which the onset of photo-current is observed is independent of the redox potential of the solution (Jaegermann and Tributsch, 1983; Mishra and Osseo-Asare, 1988a, 1988b). This finding was confirmed by photovoltaic experiments in aqueous solutions on pyrite surfaces cleaved in situ (Richardson et al., 1996).

The nature of these intrinsic surface states and the upper valence band of pyrite has been examined by synchrotron X-ray photoemission spectroscopy (Bronold et al., 1994). The valence band is comprised of bonding e_g and non-bonding t_{2g} orbitals and the conduction band is comprised of antibonding e_g^* orbitals. Thus, the upper valence band has a non-bonding character (Bronold et al., 1994; Vaughan and Craig, 1978). The surface of pyrite is characterized by an intrinsic surface state formed by iron in a square pyramidal field because of the loss of sulfur atoms. The Fe 3d orbitals are further split into two levels about 0.35 eV apart. The valence band spectra indicated that the valence band edge is close to the Fermi level, in spite of the n-type conductivity (Bronold et al., 1994). This indicates that there is an inversion layer at the pyrite surface in vacuum.

It is clear that the anodic behavior of pyrite is not that of an ideal semiconductor, nor that of a metal. The anodic dissolution of pyrite in aqueous solutions is influenced by its semiconducting nature since anodic photocurrents are observed. However, an n-type semiconductor, such as pyrite, should not readily dissolve at anodic potentials, and the Tafel slopes are not those typical of an ideal semiconductor. In semiconductor terminology, pyrite has a low breakdown potential (V_{bd} in Fig. 1) in aqueous solutions.

Although the current–voltage characteristics are an important indication of the structure of the interface (Allongue et al., 1992; Meissner and Memming, 1992), and of the charge-transfer processes occurring at the interface, the anodic current–voltage curves of pyrite

¹ All potentials are referred to the Ag/AgCl reference electrode.

have not been satisfactorily explained. In this paper, we present a study of the current–voltage characteristics of pyrite, and an XPS analysis of the surface. Finally, we propose a novel mechanism for the dissolution of n-type pyrite that describes our results.

2. Experimental apparatus and procedure

2.1. Materials and apparatus

Electrodes used were made from pyrite samples obtained from Wards Scientific Establishment, Rochester, New York. The pyrite sample was obtained in the form of single cubic crystal, which was cut into rectangles measuring approximately $1.5 \times 0.5 \times 0.5$ cm. The sample was found to be n-type by the thermoelectric method and the Hall effect method. The Hall effect measurements showed that the carrier concentration was $7.21 \pm 0.58 \times 10^{17} \text{ cm}^{-3}$. The resistivity, measured by the four-wire method, was $75 \pm 5 \times 10^{-3} \Omega \text{ cm}$. Electrical contact was made using colloidal silver paste. The pyrite was then mounted in Struers cold mounting epoxy resin leaving only one face of the pyrite exposed.

The experimental apparatus is shown in Fig. 2. A three-electrode cell was used, consisting of a pyrite working electrode, a carbon counter electrode and Ag/AgCl reference electrode. All potentials are referred to the Ag/AgCl reference. The three electrodes and the electrolyte solution were placed in a glass container fitted with a water jacket. Water from a constant water bath was pumped through the jacket. The container lid was fitted with an inlet for a gas sparger. The pyrite working electrode was connected to the rotating disk apparatus.

A BAS 100 B/W electrochemical work station, connected to a personal computer, was used to perform all voltammetry. A 1170 Solartron frequency response analyzer was used in conjunction with a 1186 Solartron electrochemical interface for the *ac*-impedance tests. The cell response was monitored for noise using a PM 3070 Philips oscilloscope.

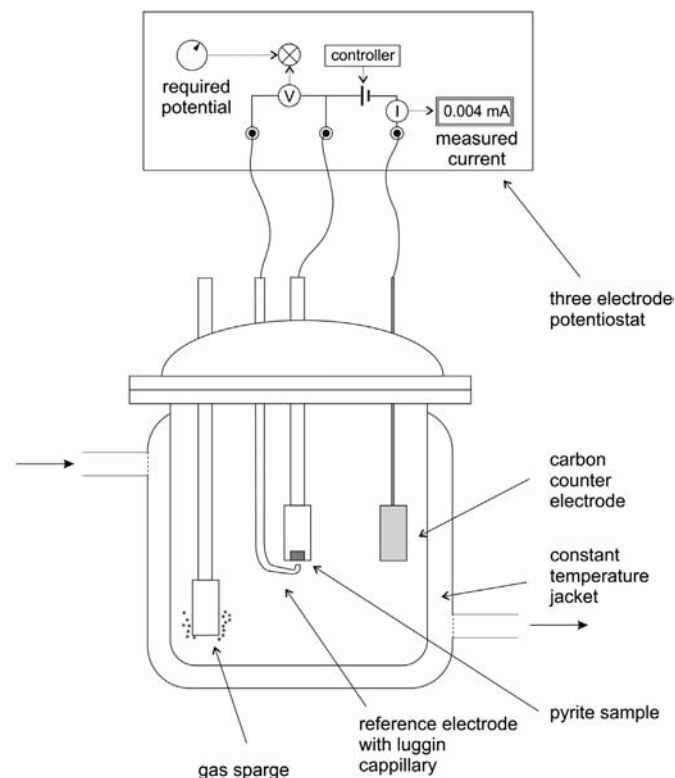


Fig. 2. The three-electrode apparatus for measures of current as a function of potential and preparing pyrite samples at particular applied potentials.

Analytical grade reagents were used throughout. High purity nitrogen gas was used.

2.2. Procedure

Nitrogen was bubbled through the solution for 15 min prior to each experiment in order to remove the dissolved oxygen. The pyrite working electrode was polished using 600 grit water paper, rinsed with deionized water and immediately immersed in the solution in the electrochemical cell. The pyrite electrode was then polarized at -0.2 V to remove any oxidation products on the surface of the pyrite electrode.

The current–voltage behavior of pyrite was investigated using steady-state and cyclic voltammetry. In the steady-state experiments, the potential of the pyrite electrode was set at an anodic potential starting at 0.7 V and held for 1 min. The potential was increased in 25 mV intervals until a potential of 1.2 V was reached.

2.3. Surface analysis

After pyrite electrodes were subjected to specified electrochemical treatment, they were removed from the electrochemical cell and thoroughly rinsed with distilled water. The pyrite sample was removed from the electrode mounting using a diamond edge metallographic sample cutter. The sample sides were still embedded in epoxy and only the treated surface and the back of the sample were exposed. The sample was dried in a nitrogen environment and transferred to a sample holder filled with nitrogen gas.

X-ray photoelectron spectroscopy (XPS) was conducted in a VG ESCALAB MK II spectrometer fitted with a VG SIMLAB. Linear background subtraction and least squares fitting procedures were used to determine peak positions, line widths and peak areas. The C 1s peak with a binding energy of 284.6 eV was used to correct data for surface charging effects. Both wide energy band and narrow energy band sweeps were carried out on the various pyrite samples.

3. Results

3.1. Current–voltage behavior

The current–voltage behavior from the rest potential to a potential of 1.2 V in solutions of three different acids is shown in Fig. 3. The data shown in Fig. 3 indicates that the type of electrolyte has little effect on the current–voltage curve.

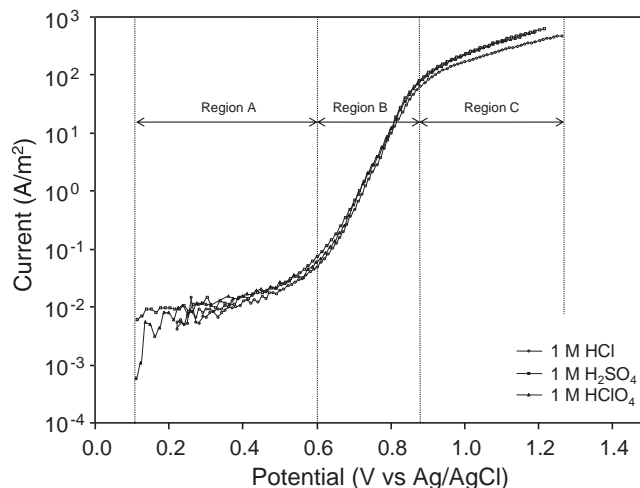


Fig. 3. The current–voltage curve for n-pyrite in different acid solutions showing the three different regions for pyrite. Conditions: temperature, 25 °C; sweep rate, 0.66 mV/s.

Three distinct regions exist for pyrite in this range of potentials. The low potential region has been referred to as the passive region by previous researchers (see for example Li and Wadsworth, 1993). This region is labeled 'A' for later reference. The intermediate potential region, labeled 'B', has a Tafel slope of about 0.09. This region has been referred to as the "transpassive", or "active" region by other researchers (Li and Wadsworth, 1993). The region above 0.9 V, labeled 'C', has not been previously discussed. The change from region 'B' to region 'C' could be caused either by a change in mechanism, or by ohmic resistance. An initial response might be to conclude that this change in slope is due to ohmic reasons. However, it is argued later from several pieces of evidence that the change in slope is not due to ohmic resistance, but to a change in mechanism.

Cyclic voltammetry at a sweep rate of 0.5 V/s confirmed that there are no anodic processes between the rest potential and 0.6 V. Two reversible processes, shown in Fig. 4 as peaks 1–1' and 2–2', occur at potentials cathodic to the rest potential, that is, at -0.1 V and 0.05 V. Conway et al. (1980) proposed that the one process corresponds with the adsorption and desorption of H^+ at the pyrite surface, and that the other process corresponds with the formation of reversible oxide layers on the pyrite surface. Mishra and Osseo-Asare (1988a, 1988b) argued that both processes are associated with the formation of oxides on the surface. A single anodic process, shown as peak 3 at potentials above 0.6 V, is the irreversible dissolution of the pyrite.

The irreversible anodic dissolution of pyrite at potentials above 0.6 V was investigated in further detail. The effect of temperature on the rate of anodic dissolution at steady state, shown in Fig. 5, is pronounced. Two regions are apparent in Fig. 5, corresponding to the regions B and C shown in Fig. 2. The average Tafel slopes are 0.082 and 0.430 V/decade for these two potential regions. Further experiments demonstrated that the rotation speed of the electrode had no effect on the current.

The effects of HCl, and KCl on the rate of anodic dissolution in regions B and C are shown in Figs. 6 and 7. The results presented in Fig. 6 indicate that the concentration of HCl has little effect on the current in a 1 M KCl solution. The results presented in Fig. 7 indicate that the concentration of KCl has a small negative effect on the current in 0.25 M HCl. The reaction order with respect to the chloride concentration is about -0.2 at 0.775 and -0.15 at 1.125 V.

The effect of electrode potential on the *ac*-impedance results are given in Figs. 8 and 9. Fig. 8 shows the Nyquist plot of the imaginary component of the impedance against the real component, while Fig. 9

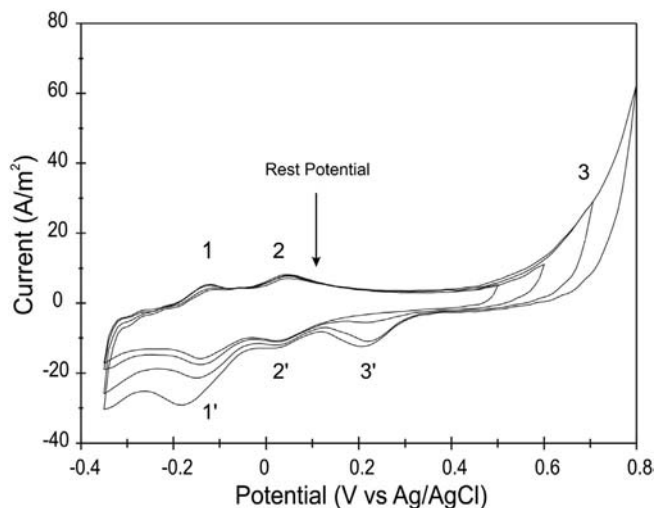


Fig. 4. The effect of sweeping to different potentials on the cyclic voltammogram of pyrite at high sweep rates. The peaks labeled 1 and 2 are reversible, due to adsorption and hydroxide formation, while peaks marked 3 are a result of the irreversible dissolution of the pyrite. Conditions: 1 M HCl; temperature, 25 °C; sweep rate, 0.5 V/s; rotation speed, 840 rpm.

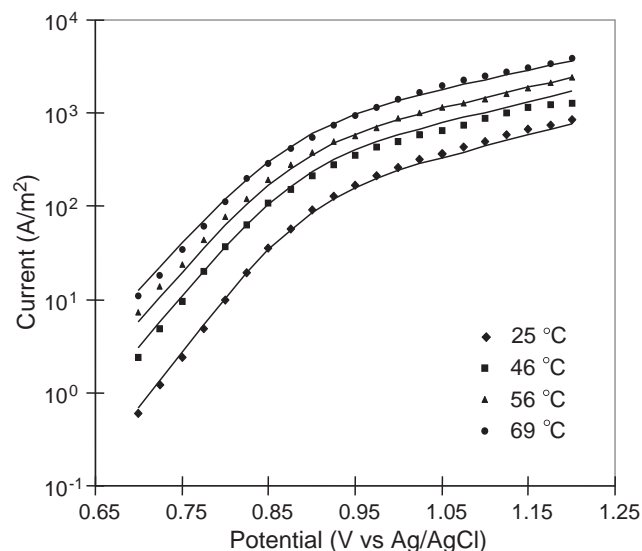


Fig. 5. The effect of temperature on the steady-state current–voltage curve of n-pyrite. The points represent the data, while the lines represent the proposed mechanism. Conditions: 1 M HCl; rotation speed, 840 rpm.

shows the amplitude and the phase angle, ϕ , as a function of frequency, $2\pi\omega$.

3.2. Surface analysis and an investigation of possible coating in the region above 0.9 V

In order to test whether the formation of a coating of reaction products in the upper region influenced the reaction kinetics, the electrode was polarized at 1.2 V for 30 min prior to the measurement of the steady-state current–voltage curve. The close correspondence of the results of this experiment with the standard pretreatment method, shown in Fig. 10, indicates that the change in Tafel slope at 0.9 V is not a result of the formation of reaction products on the surface.

Wide and narrow scan XPS spectra were obtained for pyrite samples that had been oxidized for 30 min at various anodic potentials. The surface ratio of sulfur to iron was 8.81 for the untreated pyrite. This

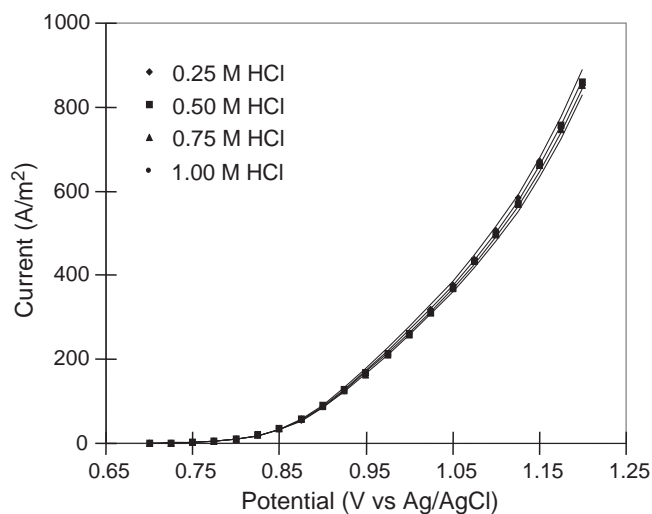


Fig. 6. The effect of the concentration of acid on the steady-state current–voltage curve of n-pyrite. The points represent the data, while the lines represent the proposed mechanism. Conditions: 1 M KCl; temperature, 25 °C; rotation speed, 840 rpm.

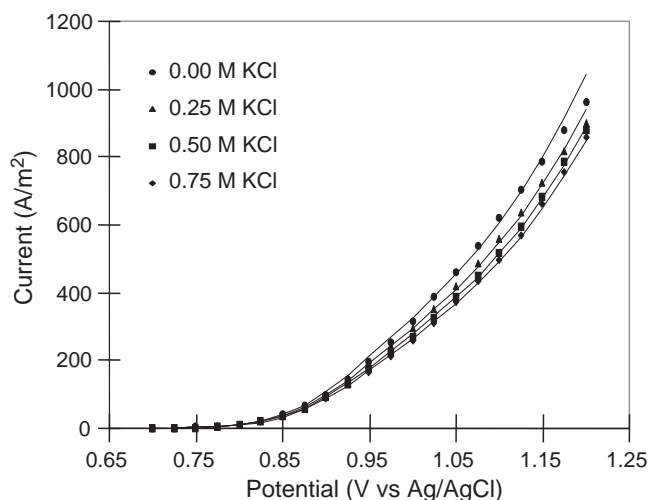


Fig. 7. The effect of the concentration of chloride ions on the steady-state current–voltage curve of n-pyrite. The points represent the data, while the lines represent the proposed mechanism. Conditions: 0.25 M HCl; temperature, 25 °C; rotation speed, 840 rpm.

ratio increased on anodic treatment. The ratios were 14.6, 13.8 and 18.5 at potentials of 0.4, 0.8 and 1.0 V, respectively. These results are similar to those of Mycroft et al. (1990) and Hyland and Bancroft (1989). In addition, it was found that the surface ratio of sulfur to iron of pyrite was 13.0 in the presence of high concentrations of chlorine. Since pyrite dissolves at high rates in the presence of chlorine, this result suggests that the sulfur enrichment of the surface does not limit the rate of anodic dissolution. This provides evidence that the change in slope at 0.9 V is not due to the formation of a coating of material on the pyrite surface.

The narrow scan spectra suggested that the S 2p peak shifted to higher binding energies. For example, the S 2p peak of the pyrite sample treated at 0.4 V had binding energy of 162.5 eV, which was the same as the untreated pyrite, while the binding energies of the peaks for the pyrite samples treated at 0.8 and 1.0 V coincided at 163.4 eV. Mycroft et al. (1990) and Hyland and Bancroft (1989) used the data of Buckley et al. (1988) to argue that the shift in binding energy of the S 2p peak is due to the formation of S_n^{2-} species. Zhu et al. (1994) also argued in favor of a polysulfide film, while Tao et al. (1994) interpreted the XPS data as suggesting the formation of a FeS-like film. The formation of polysulfide species on the surface agrees with the formation of a metal-deficient surface indicated by the wide scan data. It is again emphasized

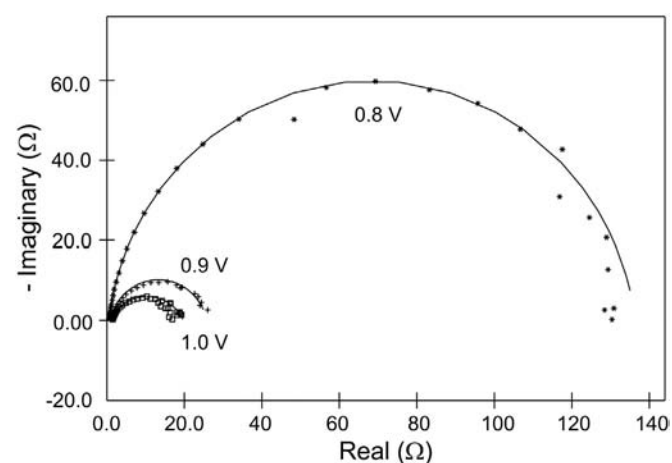


Fig. 8. The effect of pre-oxidation on the steady-state current–voltage curve of n-pyrite. Conditions: 1 M HCl; temperature, 25 °C; rotation speed, 840 rpm.

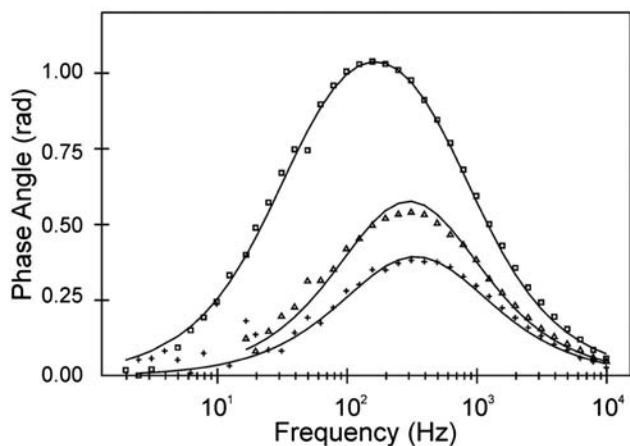
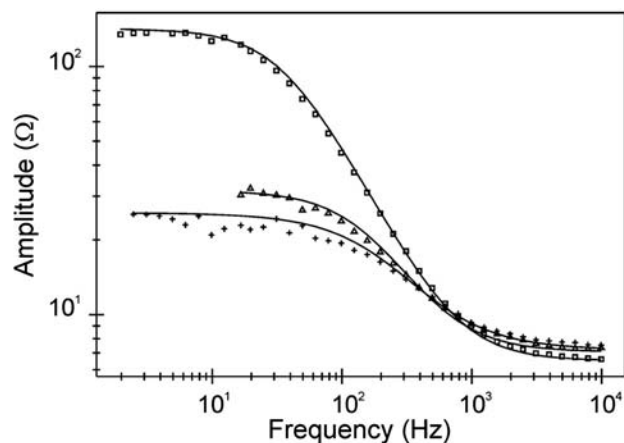


Fig. 9. Nyquist plot of the data from the ac-impedance study of pyrite at different voltages. The points represent the data, while the lines represent the proposed mechanism. The fitted constants were: 0.8 V: B 1.7e5 Ω rad, C 5.4e–5 F; 0.9 V: B 7.7e4 Ω rad, C 4.2e–5 F; 1.0 V: B 2.3e5 Ω rad, C 3.3e–5 F. Conditions: 1 M HCl; temperature, 25 °C; rotation speed, 840 rpm.

that the high currents and high rates of reaction achieved at the higher potentials and in the presence of chlorine indicate that the formation of corrosion products such as polysulfides on the pyrite surface does not limit the rate of dissolution.

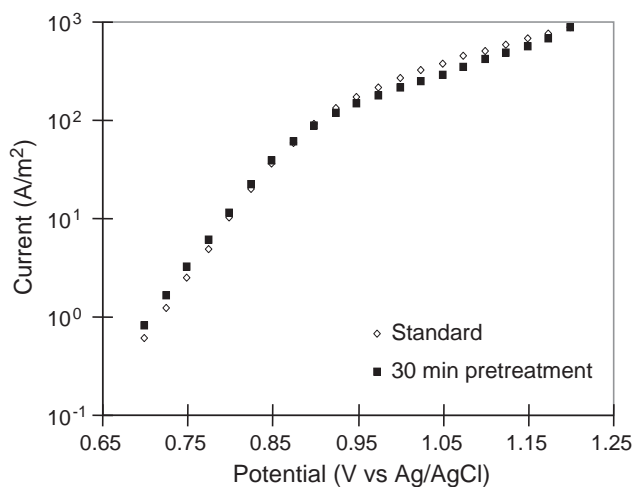


Fig. 10. Bode plot of the data from the ac-impedance study of pyrite at different voltages for the same data represented in Fig. 9. The points represent the data, while the lines represent the proposed mechanism with the same fitted constants as those in Fig. 9. Conditions: 1 M HCl; temperature, 25 °C; rotation speed, 840 rpm.

3.3. Investigation of ohmic resistance as a possible cause for the change in Tafel slope at 0.9 V

The change in slope of the current–potential curve at about 0.9 V is investigated further using three independent techniques: (i) measurement of the ohmic resistance, (ii) measurements of the mixed potential of pyrite, and (iii) measurements of the polarization resistance. The results of each of these measurements are discussed below.

The effect of ohmic resistance on the anodic current density was calculated by incorporating the potential drop across the ohmic resistance into the total potential drop in the following manner:

$$\Delta\phi = \Delta\phi_{\text{electrochemical}} + \Delta\phi_{\text{ohmic}} = \Delta\phi_{\text{electrochemical}} + iR_{\text{ohmic}} \quad (1)$$

The results of this calculation are shown in Fig. 11 using the measured resistance of the electrode of 2 Ω . If ohmic resistance is the reason for the region 'C', then the compensated curve should return to line marked 'Extrapolated' in Fig. 11. The data compensated for ohmic resistance still lies very close to the measured data, strongly suggesting that the change in slope is not caused by ohmic resistance.

In spite of the result shown in Fig. 11, it might be argued by others that the cause of the change in slope at 0.9 V is ohmic resistance because the measured resistance is too low. However, increasing the compensation for higher resistances does not return the curve to the extrapolated line representing region 'B'. Instead, it is worse – the curve is not linear at all. It has a "scorpion tail" at the higher currents. This is shown clearly in Fig. 12. Arguments based on resistance do not explain the results.

Further potent evidence is provided by the results of the mixed potential study. The mixed potential measurements are not affected by high currents (if a voltmeter with high input impedance is used). The measurements of the mixed potential of pyrite undergoing dissolution by chlorine are shown in Fig. 13. Interestingly, these measurements also reflect the same change in slope at about 0.9 V. The change in slope of the mixed potential in Fig. 13 is as a result of interfacial kinetics. This adds further support to the argument that the change in slope at 0.9 V is due to interfacial kinetics and not ohmic resistance.

The final set of evidence in favor of kinetic influences at the high current densities is the measurements of the polarization resistance obtained from low amplitude *ac*-impedance measurements. The advantage of *ac*-impedance measurements is that polarization resistance is not affected by ohmic resistance. The polarization resistance was determined from the results of the *ac*-impedance measurements using the method of McCafferty (1997). The polarization resistance is plotted as a function of potential in Fig. 14. These results also indicate a change in slope at about 0.9 V, indicating a change in kinetic behavior.

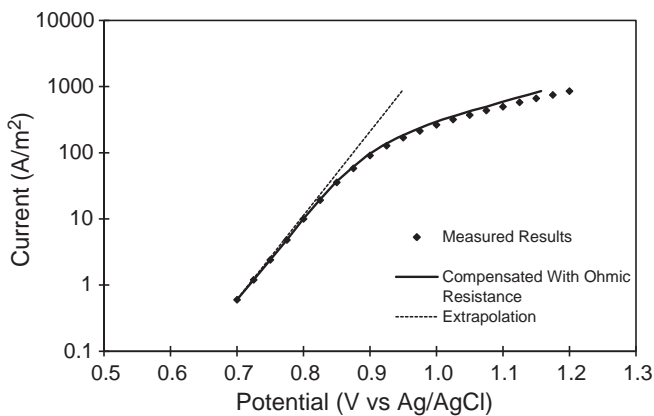


Fig. 11. The compensation of the data for an ohmic resistance of 2 Ω , showing that the measured ohmic resistance does not account for the change in Tafel slope at 0.9 V. If the change in slope were due to ohmic resistance, the compensated curve would correspond with the extrapolation of the lower region.

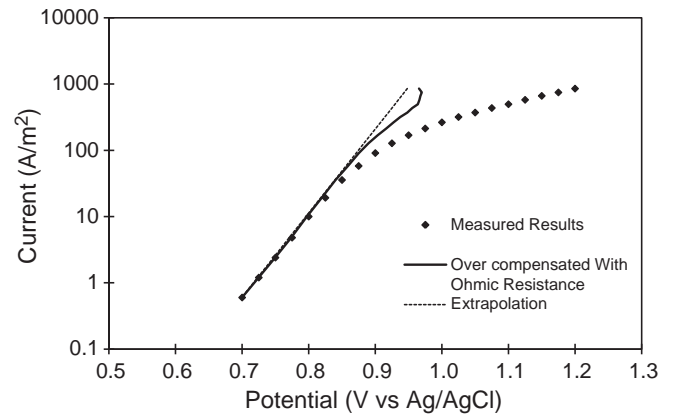


Fig. 12. Increasing the compensation for ohmic resistance to 8 Ω does not correspond with the extrapolated lower region. As the ohmic resistance is increased, the curve becomes increasingly non-linear (on a Tafel plot). This result indicates that the reason for the change in Tafel slope is not due to ohmic resistance.

Therefore, from these three sets of independent measurements, we conclude that the change in slope of the current–voltage curve at 0.9 V is due to the interfacial kinetics of pyrite.

4. Discussion

The current–voltage curves of pyrite in hydrochloric acid solutions have three anodic regions. The first region, labelled 'A' in Fig. 3, at potentials below 0.6 V, is characterized by low currents and Tafel slopes of the order of 0.3 V/decade. In the second region, which occurs at potentials between 0.6 V and 0.9 V and is labelled 'B' in Fig. 3, significant currents are measured, and the Tafel slope is between 0.075 V/decade and 0.09 V/decade. In the third region, which occurs above potentials of 0.9 V, and is labelled 'C' in Fig. 3 the current remains high; however, the Tafel slope increases to values of about 0.430 V/decade.

In the next section we present a qualitative model of the surface that accounts for the measurements presented. This qualitative model is then used to derive a quantitative mathematical model that fits the results after the next section.

4.1. Qualitative model of the interfacial surface of pyrite based on surface states with a wide distribution of energy levels

The interface between pyrite and the solution is characterized by a high density of energy states within the bandgap, both in the bulk and the surface. Bulk states are associated with Fe_2S_3 defects (Muller et al.,

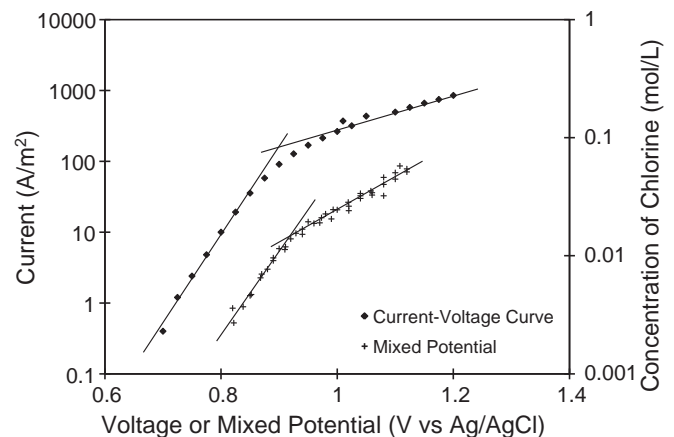


Fig. 13. The mixed potential, whose measurement does not depend on ohmic resistance, also shows the same change in slope at about 0.9 V. This result indicates that the reason for the change in Tafel slope is not due to ohmic resistance.

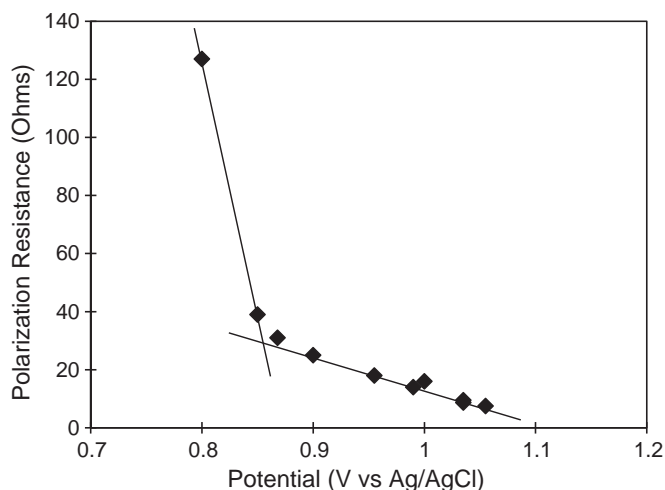


Fig. 14. The polarization resistance, which is obtained from the *ac*-impedance results, also displaces a change in slope at about 0.9 V.

1990; Salvador et al., 1991; Schubert and Tributsch, 1990), while intrinsic surface states are associated with iron d-states at the surface (Bronold et al., 1994). The surface states have a high surface density and have a relatively wide distribution of energy. In addition, surface states due to adsorption are also present on the surface of pyrite (Conway et al., 1980; Mishra and Osseo-Asare, 1988a, 1988b).

The electronic structure of the surface of pyrite that we proposed is illustrated in Fig. 15. This figure shows the electronic energy level against distance from the interface. There is a potential difference between the bulk of the solid and the surface, which results in the bending of the energy levels of the conduction and valence bands. This potential difference is shown as $\Delta\phi_{sc}$. There is also a potential difference between the interface and the outer Helmholtz plane, referred to as $\Delta\phi_H$. The overall potential measures the difference between the energy level of the bulk of the pyrite and the energy level of the reference electrode. Surface states, caused by uncompensated bonds and d-orbitals and by adsorbed solution species, are present in the band gap.

A crucial part of this model presented here is that the surface states have a relatively wide distribution of overlapping energy levels.

This model of the interface will be used to describe the measurements that were presented in the previous section.

At low potentials, the anodic current is small and has a high Tafel slope. The cyclic voltammogram at a high sweep rate confirmed that there are no anodic processes in this region. The small steady-state current in this region could be a result of a conduction band process similar to that proposed by Vanden Berghe et al. (1974). They argued that tunneling of electrons from the surface state to the conduction band was responsible for the low anodic currents of n-type CdS in the dark. For pyrite, the low current is associated with low rates of dissolution, probably caused by conduction band electrons. This explanation is illustrated in Fig. 16(a).

A change in the current–voltage curve begins at anodic potentials above 0.6 V. This change signals a change in the mechanism of charge transfer. In semiconductor terms, this potential represents the breakdown potential, where the semiconductor no longer behaves as an ideal semiconductor. As the anodic potential is increased from the rest potential, a point is reached at which the Fermi level overlaps the surface states, and significant anodic current occurs due to dissolution. This point at which the Fermi level overlaps the surface state is the breakdown potential, and heralds the onset of significant dissolution.

In this region above 0.6 V and below 0.9 V, electrons are transferred from energy levels in the surface state to the conduction band via bulk defect states, illustrated in Fig. 16(b). These defect bulk states allow charge transfer between the surface and the conduction band. In addition, the tunneling of electrons from the surface states through the energy barrier may be possible since pyrite has a high concentration of donors. Concomitant with the removal of electrons from surface bonds, bonds are broken and ions move across the Helmholtz layer to the bulk solution. The kinetics of dissolution is controlled by the transfer of electrons across the space-charge layer. However, changes in the potential are distributed across both the space-charge layer and the Helmholtz layer.

Our model for this potential region has similarities with that of Salvador et al. (1991) in the work on the n-FeS₂/I interface. They proposed that surface states and defects within the space-charge layer played an important role in the oxidation of iodide.

As the applied potential is further increased, a point is reached where the Fermi level no longer overlaps with the surface states. At

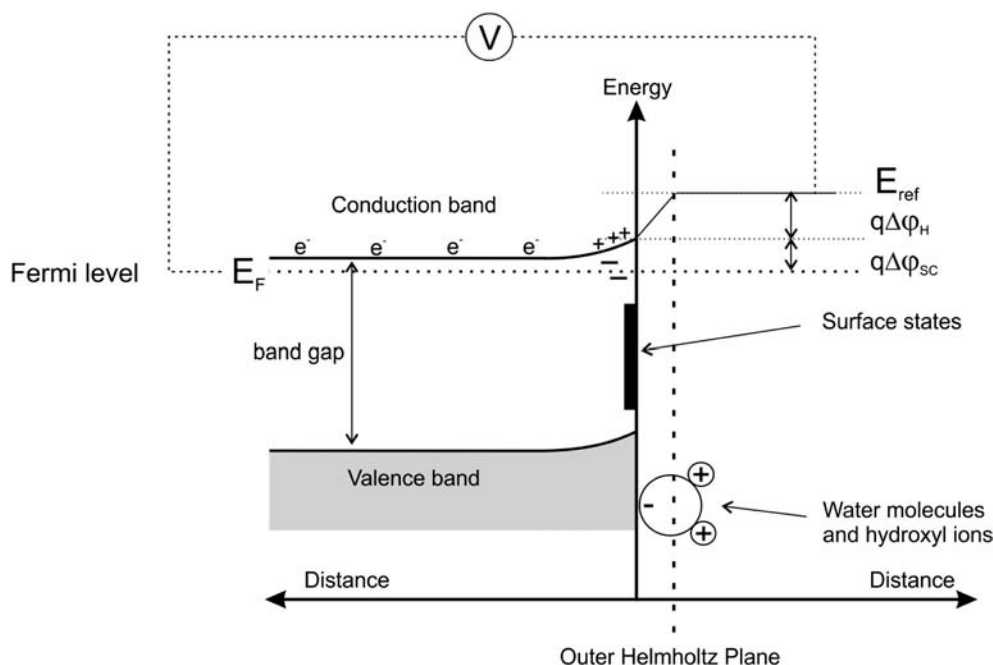


Fig. 15. The model of the pyrite interface proposed in this work.

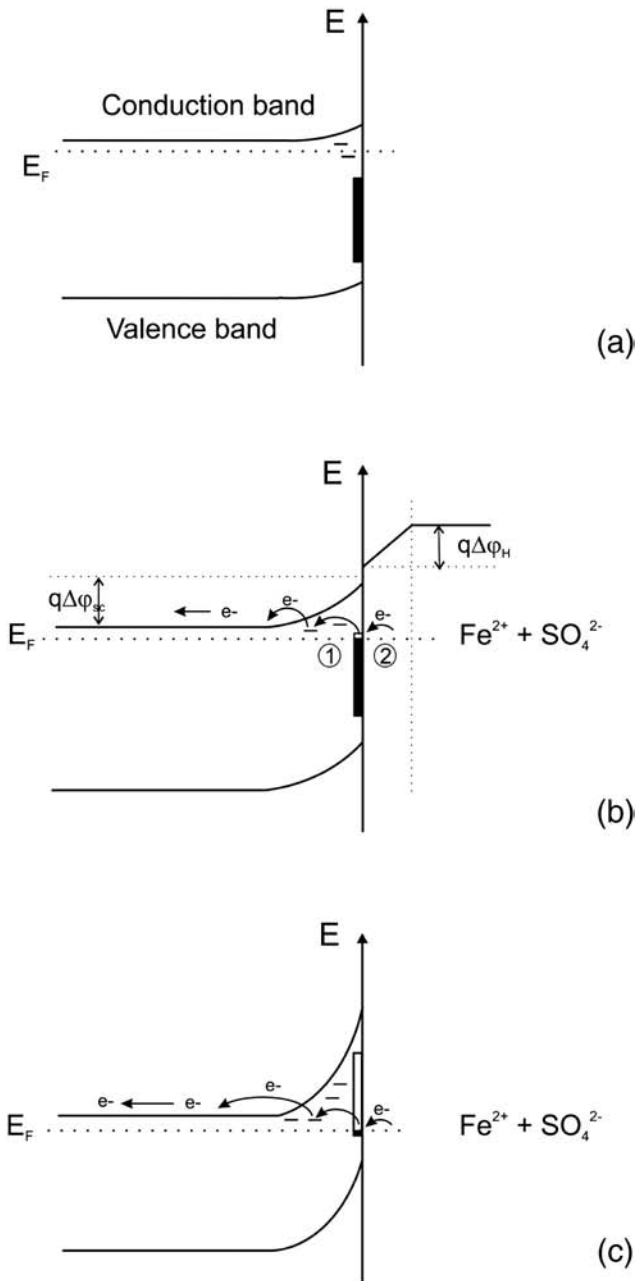


Fig. 16. Schematic diagram representing the model proposed here for the anodic behavior of n-pyrite. (a) At low potentials, the Fermi level, E_F , does not overlap with the surface state, and the behavior is typical of an n-type semiconductor, that is, there is no current due to saturation effect. Illumination increases the concentration of current carriers, and the effect of illumination in the potential region below 0.6 V has been reported. (b) At this potential, the Fermi level overlaps with the surface state, and dissolution occurs due to the holes present in the surface state. The two-steps in the mechanism are shown. Step 1 is the transfer of electrons from the surface state to the conduction band. Step 2 is the transfer of electrons from the breaking bonds at the surface to the surface state. The rate determining step is the transfer of charge across the space-charge layer. (c) At high potentials, the Fermi level is at the bottom of the surface state energy, and the occupancy of the surface state is low. The rate of anodic dissolution is controlled by the transfer of ionic species across the Helmholtz layer.

this point, the rate of electron transfer is at its maximum, and the rate of transfer of ions across the Helmholtz layer becomes the rate-limiting step. This change in the rate-controlling step results in the change in the Tafel slope at about 0.9 V shown in Figs. 3 to 9. This model of the interface is illustrated in Fig. 16(c).

This qualitative model of the interfacial kinetics is used to derive quantitative expressions for the rate of anodic dissolution of pyrite in the next section.

4.2. Quantitative mathematical model of the dissolution of pyrite

In order to describe the current–voltage behavior of pyrite quantitatively in the higher current regions, it is necessary to develop expressions that describe the rate of charge transfer for the two individual steps described above, that is, (i) the transfer between the conduction band and the surface state, and (ii) between the surface state and the solution.

The rate of transfer of electrons from the surface state to the conduction band via solid state defects is proportional to the occupancy of the surface states, f , and the band-bending in the space-charge layer, $\Delta\phi_{sc}$. This rate, j_{sc} , expressed as follows:

$$j_{sc} = k_1 s f \exp\left(\frac{F\Delta\phi_{sc}}{RT}\right) \quad (2)$$

where $\Delta\phi_{sc}$ is the potential difference across the space-charge layer, k_1 is a constant, and s is the total density of surface states.

The rate of transfer of charge across the Helmholtz layer, j_H , is given by:

$$j_H = k_2 s (1-f) \exp\left(\frac{F\Delta\phi_H}{2RT}\right) \quad (3)$$

where $\Delta\phi_H$ is the potential difference across the Helmholtz layer, and k_2 is a constant. At steady state, the rates of both these processes are equal, that is $j_{sc} = j_H = j$. Equating Eqs. (2) and (3) and solving for the surface state occupancy gives:

$$f = \frac{1}{1 + k_1/k_2 \exp((2\Delta\phi_{sc} - \Delta\phi_H)F/2RT)}. \quad (4)$$

Substituting Eq. (4) into either Eq. (2) or Eq. (3) gives an expression for the current due to anodic dissolution:

$$j = \frac{k_1 s \exp(\Delta\phi_{sc}F/RT)}{1 + k_1/k_2 \exp((2\Delta\phi_{sc} - \Delta\phi_H)F/2RT)}. \quad (5)$$

The interfacial potential difference $\Delta\phi$ is the sum of the potential difference across the space-charge layer and that across the Helmholtz layer (Allongue and Cachet, 1985; de Gryse et al., 1975; Frese and Morrison, 1979):

$$\Delta\phi = \Delta\phi_{sc} + \Delta\phi_H. \quad (6)$$

If resistance in the solution is sufficiently small, the change in the electrode potential ΔV is equal to the change in the interfacial potential difference, $\Delta\phi$. A quantitative analysis of the current–voltage curve requires a relationship between the change in the electrode potential and the change in the potential across the space-charge layer. Since the interface can be represented as the space-charge capacity in series with the Helmholtz capacity, it is possible to show that the distribution of the electrode potential ΔV over the space-charge layer and the Helmholtz layer depends only on the relative values of the capacitances (Allongue and Cachet, 1985; de Gryse et al., 1975; Frese and Morrison, 1979):

$$\Delta\phi_{sc} = \frac{C_H}{C_H + C_{sc}} \Delta V = (1-\beta)\Delta V. \quad (7)$$

The assumption is usually made that C_{sc} is much less than C_H in the study of semiconductor–solution interfaces, so that $\Delta\phi_{sc} = \Delta V$ (Salvador and Gutierrez, 1984). However, if the semiconductor is highly doped, then the space-charge capacitance is high, and the potential difference across the Helmholtz layer becomes significant. Both the space charge and the Helmholtz capacitances are functions of potential, so β in Eq. (7) is not, in general, a constant. However, Disilverstro et al.

(1986), in their study of the WO_3 interface, proposed that $d\Delta\phi_{sc} / d\Delta V$ was constant over a wide range of potential, and approximately equal to 0.2, that is, that β in Eq. (7) was 0.8. Salvador and Gutierrez (1984) found that $d\Delta\phi_H / d\Delta\phi$ was constant for n-SrTiO₃ over a potential range of 0.8 V. Vanmaekelbergh (1997) calculated values of $d\Delta\phi_H / d\Delta V$, and showed that for highly-doped semiconductors ($N_D \approx 10^{20} \text{ cm}^{-3}$) this value was about 0.4 and approximately constant with potential.

Substituting Eq. (7) into Eq. (5) gives the following expression for the current–voltage curve for the anodic dissolution of pyrite:

$$j = \frac{k_1 s \exp((1-\beta)\Delta V F / RT)}{1 + k_1/k_2 \exp((2(1-\beta)-\beta)\Delta V F / 2RT)} \quad (8)$$

Eq. (8) has two limiting cases. The first case is that at low values of the interfacial potential, under which conditions $k_1/k_2 \exp((2(1-\beta)-\beta)\Delta V F / 2RT)$ is much less than 1. In this case, the current is given by:

$$j = k_1 s \exp\left(\frac{(1-\beta)\Delta V F}{RT}\right) \quad (9)$$

A comparison of Eqs. (9) and (2) indicates that under these conditions the current is controlled by the rate of transfer of electrons from the surface state to the conduction band via defects (such as Fe_2S_3 defects) in the space-charge layer. Eq. (4) indicates that the surface state occupancy under these conditions is close to one.

The Tafel slope of the data presented in Figs. 4 to 7 is 0.082 V/decade in the low region, while that given by Eq. (9) is $2.303RT / (1-\beta)F$. Since the Tafel slope is constant, this suggests that the value of β is a constant, with a value of 0.28, over this potential range. If the value of β was equal to zero, then C_{sc} is much less than C_H and all the interfacial potential occurs across the space-charge layer. A value of 0.28 indicates that a sizeable portion of the interfacial potential occurs across the Helmholtz layer.

The second limiting case is that in which $k_1/k_2 \exp(\{2(1-\beta)-\beta\}\Delta V F / 2RT)$ is much greater than one. Under these conditions, the current is given by:

$$j = k_2 s \exp\left(\frac{\beta\Delta V F}{2RT}\right) \quad (10)$$

In this case, the transfer of charge across the Helmholtz layer is the limiting step, and the occupancy of the surface states is close to zero. Therefore, the change in Tafel slope at about 0.9 V arises because of a change in rate controlling step brought about by the surface states becoming completely unoccupied. This is illustrated in Fig. 16(c). The Tafel slope at high values of the interfacial potential difference is about 0.430 V/decade, which gives a value of β of 0.28. This value is the same as the value of β found in the first limiting case, indicating that the value of β is constant over the potential range from 0.7 to 1.2 V.

The rate constants k_1 and k_2 are Arrhenius functions of temperature. Eq. (8) may be adapted to account for the effect of temperature and the small effect of chloride ions observed. Thus, Eq. (8) becomes:

$$j = \frac{k_1' s' [\text{Cl}^-]^{-n} \exp(-E_{a1}/RT) \exp((1-\beta)\Delta V F / RT)}{1 + k_1'/k_2' \exp(-(E_{a1}-E_{a2})/RT) \exp((2(1-\beta)-\beta)\Delta V F / 2RT)} \quad (11)$$

where E_{a1} and E_{a2} are the activation energies, and $-n$ is the reaction order with respect to chloride ions.

The lines in Figs. 4 to 7 represent the fit of Eq. (11) to the data using the same parameter set for all the steady-state data. Parameters for Eq. (11) are: $k_1' s' = 4.99\text{e}9 \text{ A/m}^2 \text{ M}^{-n}$, $k_1' / k_2' = 2.63\text{e}1$, $E_{a1} = 105.3 \text{ kJ/mol}$, $E_{a1}-E_{a2} = 59.1 \text{ kJ/mol}$, $\beta = 0.275$, $n = 0.1$.

The value of the activation energy for electron transfer step is 105 kJ/mol (1.1 eV), indicative of a thermally activated surface state process. The activation energy for the transfer of charge across the Helmholtz layer is 46 kJ/mol, typical of electrochemical reactions. The values of the activation energies are consistent with the mechanism that has been proposed. The value of β was constant over the potential and temperature range. This suggests that the occupancy of the surface states that participation in the anodic dissolution process does not influence the distribution of the potential across the space charge and the Helmholtz layers.

The form of Eq. (11) suggests that chloride ions form bonds with the surface states which slightly stabilize the surface state. Other researchers have determined that the concentration of water and protons in solution affect the anodic current density (Mishra and Osseo-Asare, 1988a, 1988b, 1992), suggesting that water and protons may form bonds with surface states that affect the reactivity of the surface states.

Electrochemical impedance spectroscopy was employed in this study to determine the capacitance of the interface (Chazalviel, 1990; Tomkiewicz, 1990) in an attempt to confirm the equivalent circuit implied by Eq. (7). The impedance was modeled as a faradaic impedance, Z_f , in parallel with a capacitor, C , and a frequency dependent resistance, given by ω/B , to account for the surface roughness (Tomkiewicz, 1990). For small amplitude, sinusoidal perturbations $\tilde{V} = V_m \exp(i\omega t)$ superimposed on the electrode potential ΔV , the interfacial impedance is given by:

$$Z_f = R_t \left\{ 1 - \frac{\partial j_{sc}}{\partial \tilde{f}} \frac{\tilde{f}}{j_{sc}} \right\} \quad (12)$$

where $R_t = (\partial j_{sc} / \partial (\Delta V))^{-1}$ is the charge-transfer resistance, and \tilde{f} and \tilde{j}_{sc} are the time-dependent components of f and j , respectively. The change in occupancy of the surface states is given by the material balance:

$$e s \frac{df}{dt} = j_H - j_{sc} \quad (13)$$

Linearization and Laplace transformation of Eq. (13) yields an expression for $\tilde{f} / \tilde{j}_{sc}$. Substitution of this expression into Eq. (12), and evaluation of the partial derivative in Eq. (12) gives the following expression for the interfacial impedance:

$$Z_f = \frac{1 + k_1/k_2 \exp((\phi_1 - \phi_2)\Delta V_s)}{\phi_1 k_1 s \exp(\phi_1 \Delta V_s)} \left[\frac{i\omega e + k_2 \exp(\phi_2 \Delta V_s) + k_1 \exp(\phi_1 \Delta V_s)}{i\omega e + k_2 \exp(\phi_2 \Delta V_s) + k_1 \exp(\phi_1 \Delta V_s) \phi_2 / \phi_1} \right] \quad (14)$$

where $\phi_1 = (1-\beta)F / RT$, $\phi_2 = \beta F / 2RT$ and $i = n$. This expression can be approximated by:

$$Z_f \approx \frac{1 + k_1/k_2 \exp((\phi_1 - \phi_2)\Delta V_s)}{\phi_1 k_1 s \exp(\phi_1 \Delta V_s)} \quad (15)$$

The faradaic impedance, given by Eq. (15), is in parallel with the capacitance, C , and the frequency-dependent roughness factor, B/ω . Combination of these impedances gives a complete description of the equivalent circuit. The parameters in Eq. (15) were obtained from the steady state data. The remaining parameters in the equivalent circuit, C and B , were estimated by minimizing the sum of relative squared errors between the equivalent circuit and the impedance data. Results typical of the parameter estimation procedure are shown in Figs. 8 and 9. The lines represent the fit of the equivalent circuit to the data. The close correspondence between the data and the model lends

support to the model and the equivalent circuit, especially since the values of the reaction impedance were predicted from the parameters obtained at steady state. The values of the capacitance, however, are high, in the range of 33 to 45 $\mu\text{F}/\text{cm}^2$, and they do not follow the Mott–Schottky relationship. Pang et al. (1990) obtained values of the capacitance that were even higher, of the order of 200 $\mu\text{F}/\text{cm}^2$. They proposed that a number of layers of reaction products developed on the surface of pyrite, and these layers were responsible for their high capacitance values. In this study, no layers were detected on the surface by XPS, other than that it was enriched in sulfur. A more detailed study of the surface capacitance is recommended. In spite of this, it is clear that the model presented here predicts the interfacial impedance from the steady-state parameters.

Two other characteristics have been reported in the literature on the anodic dissolution of pyrite. They are, firstly, that the type of conductivity of pyrite does not seem to influence the Tafel slope in the potential region between 0.6 and 0.9 V (Biegler and Swift, 1979; Springer, 1970), and, secondly, that illumination increases the anodic current density (Chen et al., 1991; Ennaoui et al., 1985, 1986; Mishra and Osseo-Asare, 1992; Schubert and Tributsch, 1990). At first, these two observations seem contradictory, since the first indicates that the semiconducting nature of pyrite is not important, while the second indicates that it is important. The mechanism of anodic dissolution that is presented here can account for both of these observations, as discussed below.

4.3. Influence of the type of conductivity of pyrite

Both Springer (1970) and Biegler and Swift (1979) found that the type of conductivity did not influence the current–voltage characteristics of pyrite. The proposed mechanism of the anodic dissolution of p-type pyrite is shown in Fig. 17. The charge transfer process is the transfer of the majority carriers, holes for p-type semiconductors, from the valence band edge to the surface state. The rate of this process is proportional to the concentration of holes at the surface, and the occupancy of the surface state. Since the concentration of holes at the surface is dependent on the potential difference across the space-charge layer, the rate of this process is given by:

$$j_{sc} = k_p p_b s f \exp\left(\frac{F\Delta\phi_{sc}}{RT}\right) \quad (16)$$

where p_b is the density of holes in the bulk pyrite. The rate of transport of ions from the surface to the solution across the Helmholtz layer is given by Eq. (4). Therefore, by following the same method as used in the

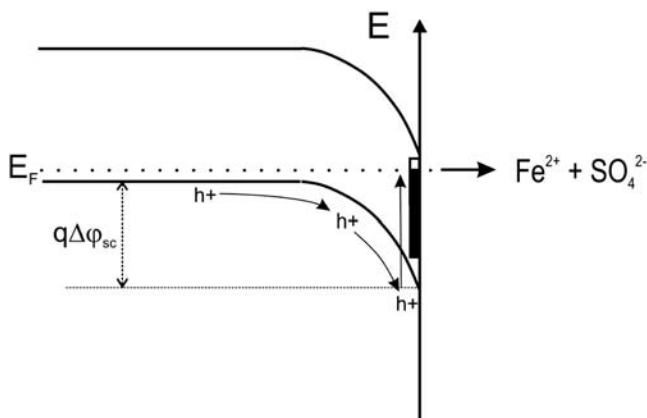


Fig. 17. The effect of the surface state on the dissolution of p-type pyrite is similar to that of n-type pyrite. In this case the charge carriers are holes that move from the bulk across the space-charge layer.

derivation of Eq. (8) above, the current due to anodic dissolution of p-type pyrite is found to be:

$$j = \frac{k_p p_b s \exp((1-\beta)\Delta V F / RT)}{1 + k_p / k_2 \exp((2(1-\beta) - \beta)\Delta V F / 2RT)} \quad (17)$$

It is clear that Eq. (17) is of the same form as Eq. (8), and the Tafel slopes are the same. Therefore, the mechanism of the anodic dissolution of pyrite is not dependent on the type of conductivity. It would be most interesting to determine if p-type pyrite displays the change in Tafel slope above 0.9 V described in this work, and to determine the activation energies for the constant k_p .

4.4. Influence of illumination on the anodic dissolution of pyrite

A number of researchers have found that both natural and synthetic pyrite display photoeffects. Jaegermann and Tributsch (1983) reported photocurrents in the anodic potential region. They determined a band gap of 0.9 eV from the photocurrent spectra. They argued that the reaction of photogenerated holes with water leads to corrosion, with SO_4^{2-} as the corrosion product. They also observed a shift in the flat-band potential, caused by surface states or inter-bandgap states. They proposed a model of the interface that accounts for their measurements. Their model assumed that the presence of the high density of surface states resulted in all the change in the potential difference occurring across the Helmholtz layer, that is, the Fermi level is pinned. The photogenerated holes reacted with the reductant in solution, generating a sustained photocurrent.

The model of the interface proposed by Jaegermann and Tributsch (1983) is similar to that proposed here. However, we propose that the potential is distributed across both the Helmholtz and the space-charge layer. Our model of the effect of illumination is shown in Fig. 18.

Illumination causes electrons to be excited from the valence band to the conduction band. This creates electrons in the conduction band, and holes in the valence band. Electrons in the conduction band migrate to the external circuit, while the holes left behind migrate to the surface. The holes at the surface have two different options: (i) they can either react directly with bonding orbitals to cause dissolution, or (ii) they can join the surface state, thus lowering the Fermi energy, indirectly causing dissolution.

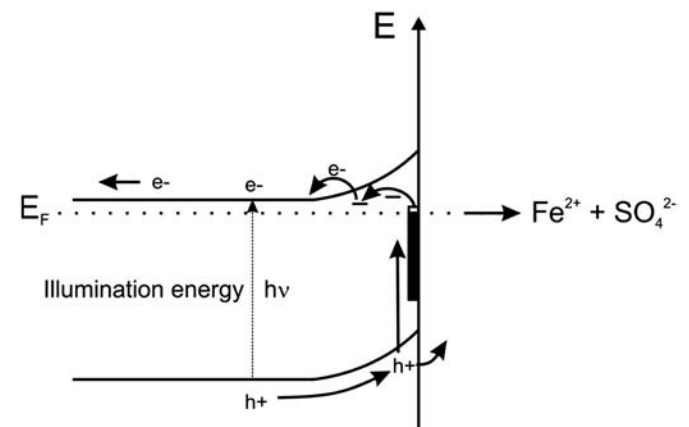


Fig. 18. The effect of illumination on n-pyrite. Illumination increases the concentration of holes and electrons. The electrons are transported to the external circuit where they increase the current. The holes are transported to the surface where either they react with species in solution or they react with the surface state and increase the rate of anodic dissolution. This model indicates that illumination will increase the anodic current over the entire potential range.

Mishra and Osseo-Asare (1992) found that illumination increased the anodic current in the whole potential region. This result is consistent with our model. We propose that the behavior of pyrite is that of an ideal n-type semiconductor in the low potential region (below 0.6 V). Above this potential, significant corrosion occurs. In the potential region above 0.6 V, the photogenerated holes are captured by the surface state, the reaction of the surface state results in corrosion. Thus, effect of the illumination is to increase the current in the anodic region. The recombination of photogenerated electron-hole pairs and the capture of holes by solution species also occur at the pyrite-solution interface.

Thus, our model accounts for the shift in the flat-band potential and the effect of illumination over the entire anodic region.

5. Conclusions

We studied the anodic electrochemistry of n-type pyrite from the rest potential to 1.2 V (vs Ag/AgCl). Three regions exist in the steady-state data: at potentials between the rest potential and 0.6 V, the current is low; at potentials between 0.6 V and 0.9 V, significant currents are measured, and the Tafel slope is about 0.082 V/decade; and at potentials above 0.9 V, the Tafel slope changes to about 0.430 V/decade. This basic shape of the current-voltage curve was the same in hydrochloric, sulfuric and nitric acids. It was shown that the change in Tafel slope at about 0.9 V is not due to the formation of surface coatings, nor is it an artifact of the resistivity of the pyrite.

We proposed a comprehensive mechanism for the anodic behavior of pyrite in aqueous solutions that accounts for these three regions. In the low potential region, the behavior of pyrite is typical of a highly doped n-type semiconductor. At increased potentials (above 0.6 V), the Fermi level overlaps the energy levels of the surface states, and significant current flows. The current is controlled by the transfer of electrons from the surface state to the conduction band via bulk defects within the space-charge layer. As the potential is further increased (above 0.9 V), the Fermi level no longer overlaps with the surface states, and the kinetics of dissolution is controlled by the transfer of ions across the Helmholtz layer. The model is able to describe both the steady-state data, and the charge-transfer resistance from the data using electrochemical impedance spectroscopy. The model can also be used to explain why n-type and p-type pyrite samples have the same value of the Tafel slope and why illumination increases the anodic current, two seemingly contradictory observations.

References

- Ahlberg, E., Broo, A.E., 1997. Electrochemical reaction mechanisms at pyrite in acid perchlorate solutions. *J. Electrochem. Soc.* 144, 1281–1286.
- Allongue, P., Cachet, H., 1985. Band-edge shift and surface charge at illuminated n-GaAs/ aqueous electrolyte junctions. *J. Electrochem. Soc.* 132, 45–52.
- Allongue, P., Blonkowski, S., Souteyrand, E., 1992. Experimental investigation of charge transfer at the semiconductor/electrolyte junction. *Electrochim. Acta* 37, 781–797.
- Bard, A.J., Bocarsly, A.B., Fan, F.-R.F., Walton, E.G., Wrighton, M.S., 1980. The concept of Fermi-level pinning at semiconductor/liquid junctions. *J. Am. Chem. Soc.* 102, 3671–3677.
- Biegler, T., Swift, D.A., 1979. Anodic behavior of pyrite in acidic solutions. *Electrochim. Acta* 24, 415–420.
- Bronold, M., Tomm, Y., Jaegermann, W., 1994. Surface states on cubic d-band semiconductor pyrite (FeS₂). *Surf. Sci. Lett.* 314, L931–L936.
- Buckley, A.N., Wouterlood, H.J., Cartwright, P.S., Gillard, R.D., 1988. Core electron binding energies of platinum and rhodium polysulphides. *Inorg. Chim. Acta* 143, 77–80.
- Chazalviel, J.-N., 1982. Electrochemical transfer via surface states: a new formulation for the semiconductor/electrolyte interface. *J. Electrochem. Soc.* 129, 963–969.
- Chazalviel, J.-N., 1990. Impedance studies at semiconductor electrodes: classical and more exotic techniques. *Electrochim. Acta* 35, 1545–1552.
- Chen, G., Zen, J., Fan, F.F., Bard, A.J., 1991. Electrochemical investigation of the energetics of irradiated FeS₂ (pyrite) particles. *J. Phys. Chem.* 95, 3682–3687.
- Conway, B.E., Ku, J.C.H., Ho, F.C., 1980. The electrochemical surface reactivity of iron sulphide, FeS₂. *J. Colloid Interface Sci.* 75, 357–372.
- Crundwell, F.K., 1988. The influence of electronic structure of solids on the anodic dissolution and leaching of semiconducting sulphide minerals. *Hydrometallurgy* 21, 155–190.
- De Gryse, R., Gomes, W.P., Cardon, F., Vennik, J., 1975. On the interpretation of the Mott-Schottky plots determined at semiconductor/electrolyte systems. *J. Electrochem. Soc.* 122, 711–712.
- Dew, D.W., Lawson, E.N., Broadhurst, J.L., 1997. In: Rawlings, D.E. (Ed.), *Biomining: Theory, Microbes and Industrial Processes*. Springer, Berlin, pp. 45–80 (1997).
- Disilverstro, J., Gratzel, M., Pajkossy, T., 1986. Electron transfer at the WO₃-electrolyte interface under controlled mass transfer conditions. *J. Electrochem. Soc.* 133, 331–336.
- Doyle, F.M., Mirza, A.H., 1996. In: Woods, R., Doyle, F.M., Richardson, P. (Eds.), *Electrochemistry in Mineral and Metal Processing IV*. The Electrochemical Society, Pennington, N.J.
- Ennaoui, A., Fiechter, S., Goslowsky, H., Tributsch, H., 1985. Photoactive synthetic polycrystalline pyrite (FeS₂). *J. Electrochem. Soc.* 132, 1579–1582.
- Ennaoui, A., Fiechter, S., Jaegermann, W., Tributsch, H., 1986. Photoelectrochemistry of high quantum efficient single crystalline n-FeS₂ (pyrite). *J. Electrochem. Soc.* 133, 97–106.
- Evangelou, V.P., 1995. *Pyrite Oxidation and its Control*. CRC Press, Boca Raton.
- Fowler, T.A., Holmes, P.R., Crundwell, F.K., 1999. Mechanism of pyrite dissolution in the presence of *Thiobacillus ferrooxidans*. *Appl. Environ. Microbiol.* 65, 2987–2993.
- Fowler, T.A., Holmes, P.R., Crundwell, F.K., 2001. On the kinetics and mechanism of the dissolution of pyrite in the presence of *Thiobacillus ferrooxidans*. *Hydrometallurgy* 59, 257–270.
- Frank, S.N., Bard, A.J., 1975. Semiconductor electrodes. II Electrochemistry at n-type TiO₂ electrodes in acetonitrile solutions. *J. Am. Chem. Soc.* 97, 7427–7434.
- Frese Jr., K.W., Morrison, S.R., 1979. Electrochemical measurements of interface states at the GaAs/oxide interface. *J. Electrochem. Soc.* 126, 1235–1241.
- Holmes, P.R., Crundwell, F.K., 2000. The kinetics of the oxidation of pyrite by ferric ions and dissolved oxygen: an electrochemical study. *Geochim. Cosmochim. Acta* 64, 263–274.
- Holmes, P.R., Fowler, T.A., Crundwell, F.K., 1999. The mechanism of the bacterial leaching of pyrite: an electrochemical study. *J. Electrochem. Soc.* 146, 2906–2912.
- Hyland, M.M., Bancroft, G.M., 1989. An XPS study of gold deposition at low temperatures on sulphide minerals: reducing agents. *Geochim. Cosmochim. Acta* 53, 367–372.
- Jaegermann, W., Tributsch, H., 1983. Photo electrochemical reactions of FeS₂ (pyrite) with H₂O and reducing agents. *J. Appl. Electrochem.* 13, 743–750.
- Kohl, P.A., Bard, A.J., 1977. Semiconductor electrodes. 13. Characterization and behavior of n-type zinc oxide, cadmium sulfide, and gallium phosphide electrodes in acetonitrile solutions. *J. Am. Chem. Soc.* 99, 7531–7539.
- Koval, C.A., Howard, J.N., 1992. Electron transfer at semiconductor electrode-liquid electrolyte interfaces. *Chem. Rev.* 92, 411–433.
- Li, J., Peter, L.M., 1985. Surface recombination at semiconductor electrodes. Part III. Steady state and intensity modulated photocurrent response. *J. Electroanal. Chem.* 193, 27–47.
- Li, J., Wadsworth, M.E., 1993. In: Hiskey, J.B., Warren, G.W. (Eds.), *Hydrometallurgy: Fundamentals, Technology and Innovation*. SME, pp. 127–141.
- McCafferty, E., 1997. On the determination of distributed double-layer capacitances from Cole-Cole plots. *Corrosion Sci.* 39, 243–254.
- Meissner, D., Memming, R., 1992. Analysis of current-potential characteristics at n- and p-type semiconductor electrodes. *Electrochim. Acta* 37, 799–809.
- Meyer, R.E., 1979. Electrochemistry of FeS₂. *J. Electroanal. Chem.* 101, 59–71.
- Mishra, K.K., Osseo-Asare, K., 1987. Photodissolution of coal pyrite. *Fuel* 66, 1161–1163.
- Mishra, K.K., Osseo-Asare, K., 1988a. Aspects of the interfacial electrochemistry of semiconductor pyrite (FeS₂). *J. Electrochem. Soc.* 135, 2502–2509.
- Mishra, K.K., Osseo-Asare, K., 1988b. Electrodeposition of H⁺ on oxide layers at pyrite (FeS₂) surfaces. *J. Electrochem. Soc.* 135, 1898–1901.
- Mishra, K.K., Osseo-Asare, K., 1992. Fermi level pinning at pyrite (FeS₂)/electrolyte junctions. *J. Electrochem. Soc.* 139, 749–752.
- Morrison, S.R., 1980. *Electrochemistry at Semiconductor and Oxidized Metal Electrodes*. Plenum Press, N.Y.
- Muller, W., Bertschat, H.H., Biedermann, K., Kowalik, R., Lahmer-Naim, E., Mahnke, H.-E., Seeger, S., Zeitz, W.-D., Feichter, S., Tributsch, H., 1990. Perturbed-angular-distribution measurements of the chemical shift of iron in the disulfides FeS₂ (pyrite) and RuS₂ (laurite). *Phys. Rev. B* 41, 8624–8629.
- Mycroft, J.R., Bancroft, G.M., McIntyre, N.S., Lorimer, J.W., Hill, I.R., 1990. Detection of sulphur and polysulphides on electrochemically oxidized pyrite surfaces by X-ray photoelectron spectroscopy and Raman spectroscopy. *J. Electroanal. Chem.* 209, 139–152.
- Noufi, R.N., Kohl, P.A., Frank, S.N., Bard, A.J., 1978. Semiconductor electrodes. XIV. Electrochemistry and electroluminescence at n-type TiO₂ in aqueous solutions. *J. Electrochem. Soc.* 125, 246–252.
- Pang, J., Briceno, A., Chandler, S., 1990. Study of pyrite/solution interface by impedance spectroscopy. *J. Electrochem. Soc.* 137, 3447–3455.
- Peters, E., Majima, H., 1967. Electrochemical reactions of pyrite in acidic perchlorate solutions. *Can. Metall. Q.* 7, 111–117.
- Reichman, J., 1980. The current-voltage characteristic of semiconductor-electrolyte junction photovoltaic cells. *Appl. Phys. Lett.* 36, 574–577.
- Richardson, P.E., Yoon, R.H., Mendiratta, N.K., 1996. In: Woods, R., Doyle, F.M., Richardson, P. (Eds.), *Electrochemistry in Mineral and Metal Processing IV*. The Electrochemical Society, Pennington, N.J.
- Salvador, P., Gutierrez, C., 1984. Mechanisms of charge transfer at the semiconductor-electrolyte interface. *J. Electrochem. Soc.* 131, 326–336.
- Salvador, P., Tafalla, D., Tributsch, H., Wetzel, H., 1991. Reaction mechanisms at the n-FeS₂/I interface: an electrolyte electroreflectance study. *J. Electrochem. Soc.* 138, 3361–3369.
- Schubert, B., Tributsch, H., 1990. Photoinduced electron transfer by coordination chemical pathways across pyrite electrolyte interfaces. *Inorg. Chem.* 29, 5041.

- Springer, G., 1970. Observations on the electrochemical reactivity of semiconducting minerals. *Trans. Inst. Min. Metall. C* 79, C11–C15.
- Tao, D.P., Li, Y.Q., Richardson, P.E., Yoon, R.-H., 1994. The incipient oxidation of pyrite. *Colloids Surf. A* 93, 229–239.
- Tomkiewicz, M., 1990. Impedance spectroscopy of rectifying semiconductor–electrolyte interfaces. *Electrochim. Acta* 35, 1631–1635.
- Vanden Berghe, R.A.L., Cardon, F., Gomes, W.P., 1974. Electron transfer involving tunneling from surface states at the dark anodic CdS/indifferent electrolyte interface. *Ber. Bunsenges.* 78, 331–335.
- Vandermolen, J., Gomes, W.P., Cardon, F., 1980. Investigation of the kinetics of electroreduction processes at dark TiO₂ and SrTiO₃ single crystal semiconductor electrodes. *J. Electrochem. Soc.* 127, 324–328.
- Vanmaekelbergh, D., 1997. Direct and surface state mediated electron transfer at semiconductor/electrolyte junctions – I. A comparison of steady-state results. *Electrochim. Acta* 42, 1121–1134.
- Vaughan, D.J., Craig, J.R., 1978. *Mineral Chemistry of Metal Sulphides*. Cambridge University Press.
- Wei, D., Osseo-Asare, K., 1996. Semiconductor electrochemistry of particulate pyrite: dissolution via hole and electron pathways. *J. Electrochem. Soc.* 143, 3192–3198.
- Wei, D., Osseo-Asare, K., 1997. Semiconductor electrochemistry of particulate pyrite: mechanisms and products of dissolution. *J. Electrochem. Soc.* 144, 546–553.
- Zhu, X., Lu, J., Wadsworth, M.E., 1994. Characterization of surface layers formed during pyrite oxidation. *Colloids Surf. A* 93, 201–210.